JACS
JOURNAL OF THE AMERICAN CHEMICAL SOCIETY
Article
pubs.acs.org/JACS

A General Approach to Preferential Formation of Active Fe−N_x Sites in Fe−N/C Electrocatalysts for Efficient Oxygen Reduction Reaction

Young Jin Sa,[†] Dong-Jun Seo,[§] Jinwoo Woo,[‡] Jung Tae Lim,[⊥] Jae Yeong Cheon,[†] Seung Yong Yang,[§] Jae Myeong Lee,[§] Dongwoo Kang,[†] Tae Joo Shin,[∥] Hyeon Suk Shin,[†] Hu Young Jeong,[∥] Chul Sung Kim,[*,⊥] Min Gyu Kim,[*,#] Tae-Young Kim,[*,§] and Sang Hoon Joo[*,†,‡]

[†]Department of Chemistry and [‡]School of Energy and Chemical Engineering, Ulsan National Institute of Science and Technology (UNIST), 50 UNIST-gil, Ulsan 44919, Republic of Korea

[§]Hydrogen and Fuel Cell Center, Korea Institute of Energy Research (KIER), Jellabuk-do 56332, Republic of Korea

[∥]UNIST Central Research Facility, Ulsan National Institute of Science and Technology (UNIST), 50 UNIST-gil, Ulsan 44919, Republic of Korea

[#]Beamline Division, Pohang Accelerator Laboratory, Pohang, Kyungbuk 37673, Republic of Korea

[⊥]Department of Physics, Kookmin University, Seoul 02707, Republic of Korea

Supporting Information

ABSTRACT: Iron−nitrogen on carbon (Fe−N/C) catalysts have emerged as promising nonprecious metal catalysts (NPMCs) for oxygen reduction reaction (ORR) in energy conversion and storage devices. It has been widely suggested that an active site structure for Fe−N/C catalysts contains Fe−N_x coordination. However, the preparation of high-performance Fe−N/C catalysts mostly involves a high-temperature pyrolysis step, which generates not only catalytically active Fe−N_x sites, but also less active large iron-based particles. Herein, we report a general "silica-protective-layer-assisted" approach that can preferentially generate the catalytically active Fe−N_x sites in Fe−N/C catalysts while suppressing the formation of large Fe-based particles. The catalyst preparation consisted of an adsorption of iron porphyrin precursor on carbon nanotube (CNT), silica layer overcoating, high-temperature pyrolysis, and silica layer etching, which yielded CNTs coated with thin layer of porphyrinic carbon (CNT/PC) catalysts. Temperature-controlled in situ X-ray absorption spectroscopy during the preparation of CNT/PC catalyst revealed the coordination of silica layer to stabilize the Fe−N_4 sites. The CNT/PC catalyst contained higher density of active Fe−N_x sites compared to the CNT/PC prepared without silica coating. The CNT/PC showed very high ORR activity and excellent stability in alkaline media. Importantly, an alkaline anion exchange membrane fuel cell (AEMFC) with a CNT/PC-based cathode exhibited record high current and power densities among NPMC-based AEMFCs. In addition, a CNT/PC-based cathode exhibited a high volumetric current density of 320 A cm^{-3} in acidic proton exchange membrane fuel cell. We further demonstrated the generality of this synthetic strategy to other carbon supports.

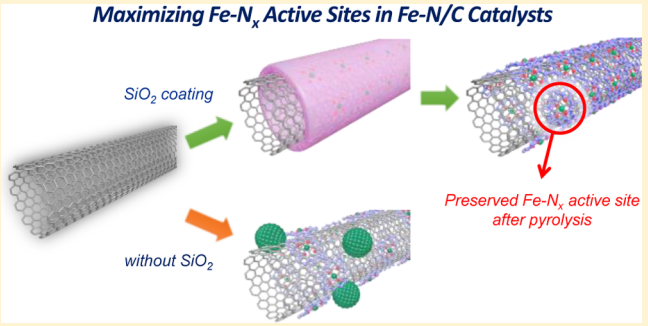

INTRODUCTION

Polymer electrolyte fuel cells (PEFCs) represent one of the most promising energy conversion devices available today, because of their high energy conversion efficiency and zero emission of greenhouse gases.[1−6] However, the high cost and scarcity of platinum pose a great challenge to the widespread adoption of PEFC technologies. Particularly for acidic proton exchange membrane fuel cells (PEMFCs) where Pt-based catalysts are primarily used in both the cathode and the anode, these catalysts are solely responsible for 40−50% of the total cost of the PEMFC stack.[7,8] As an alternative type of PEFCs, anion exchange membrane fuel cells (AEMFCs) incorporating solid alkaline electrolytes have received increasing attention during the past few years.[9,10] In particular, the higher oxygen reduction reaction (ORR) activity and enhanced durability of low-cost nonprecious metal catalysts (NPMCs) in alkaline media than in acidic media have prompted the current surge of interest in AEMFC as an economically viable energy conversion device. In this context, a wide range of NPMCs, including transition metal and nitrogen codoped carbons (M−N/C),[11−41] metal-free heteroatom-doped carbons,[42−48] and metal oxide-carbon composites,[49−52] have been investigated for replacing Pt-based catalysts. Among NPMCs, the Fe−N/C catalysts especially have emerged as the most promising ORR catalysts due to their high ORR activity.[11−35] Despite of recent progress in Fe−N/C catalysts, their implementation in single

Received: September 8, 2016
Published: October 18, 2016

DOI: 10.1021/jacs.6b09470
J. Am. Chem. Soc. 2016, 138, 15046−15056

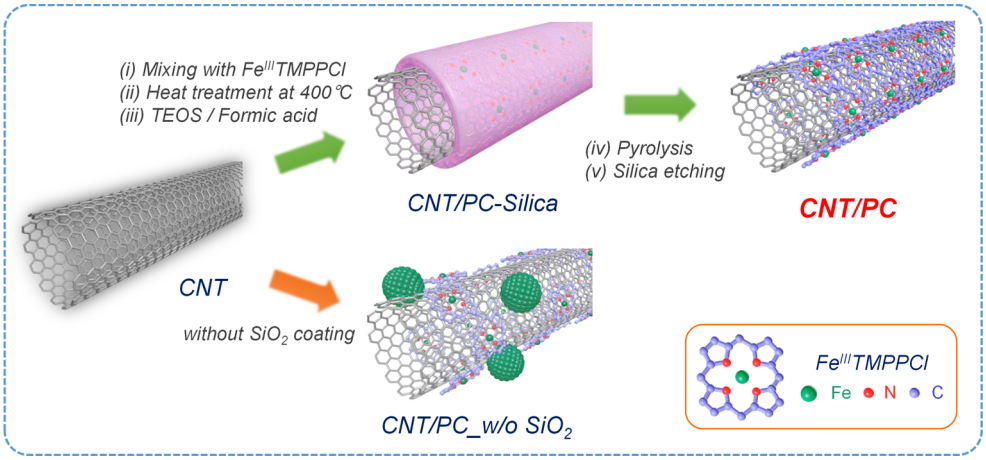

Figure 1. Synthetic scheme for the preparation of CNT/PC catalysts.

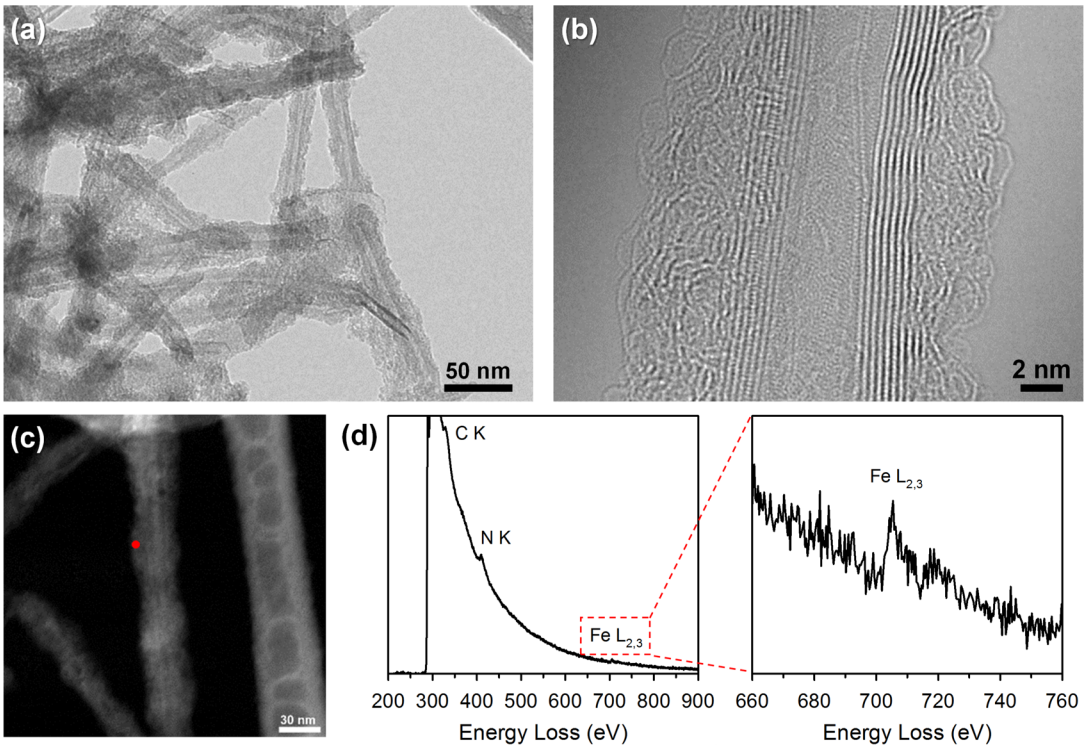

Figure 2. (a) TEM and (b) AR-TEM images of CNT/PC. (c) HAADF-STEM image and (d) EELS spectrum of CNT/PC taken at red spot of HAADF-STEM image.

cells has been predominantly limited to PEMFCs, and has lagged far behind for AEMFCs.

In parallel with efforts to enhance the ORR activity, significant advances have been made to decipher the structure of the active sites of Fe−N/C catalysts. A growing body of literature based on spectroscopic studies suggests that the active site of these catalysts involve Fe−N_x coordination, thus providing the scientific basis for designing highly active Fe−N/C catalyst.[53−68] However, a rational design strategy that can preferentially generate active Fe−N_x sites yet to be explored. Most synthetic approaches to Fe−N/C catalysts involve a high-temperature pyrolysis step to endow conductivity and stability to the catalysts. However, this step generates not only catalytically active Fe−N_x sites, but also a significant amount of less-active large Fe-based particles. Therefore, additional synthetic steps including post acid- and heat-treatments are commonly required to boost the ORR activity.[32,35]

Herein, we report a generalized "silica-protective-layer-assisted" strategy that can preferentially produce catalytically active Fe−N_x sites during high-temperature pyrolysis toward highly efficient Fe−N/C electrocatalysts (Figure 1). The catalyst synthesis involved an adsorption of porphyrinic precursor on carbon nanotube (CNT), silica layer overcoating, high-temperature pyrolysis, and silica layer etching, yielding the nanocomposite structure of CNT coated with thin layer of porphyrinic carbon (CNT/PC). We point out that while "silica coating" strategy has been widely used in catalysis for mitigating the sintering of catalytic particles under high-temperature and/or harsh reaction conditions,[69−73] in our work this method is exploited to promote the formation of catalytically active sites at the molecular level. Temperature-controlled in situ X-ray

DOI: 10.1021/jacs.6b09470
J. Am. Chem. Soc. 2016, 138, 15046−15056

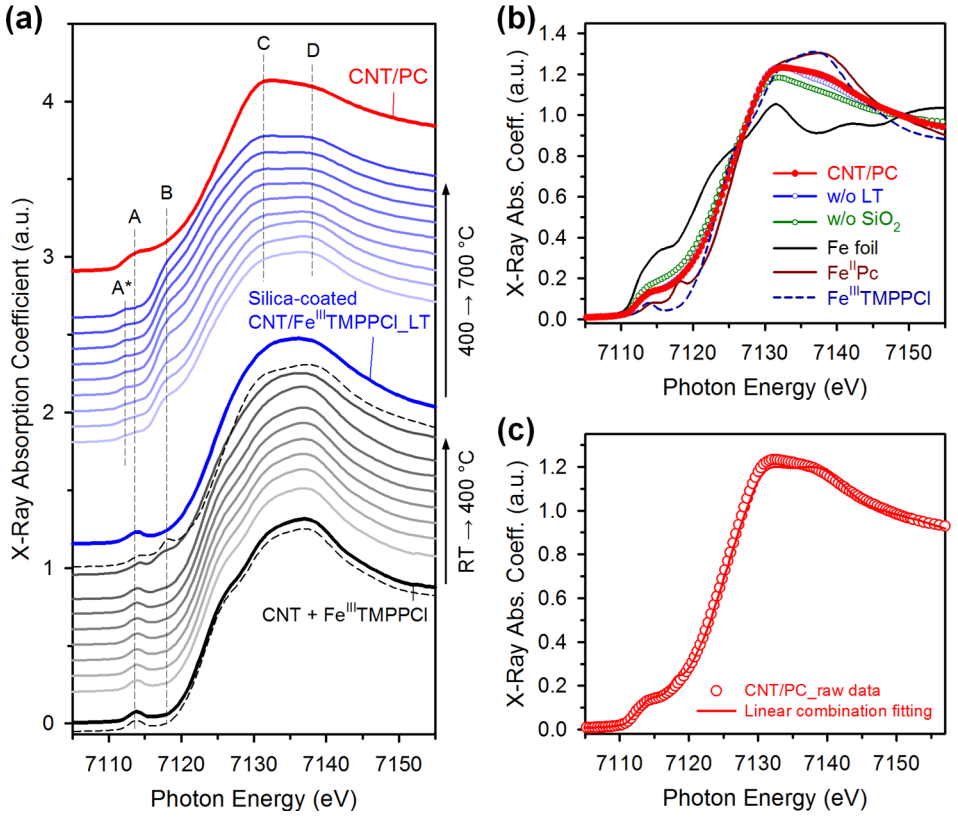

Figure 3. (a) Temperature-dependent Fe K-edge XANES spectra during two-step pyrolysis of CNT/PC; dashed lines indicate the XANES spectra of Fe^{III}TMPPCl (bottom) and Fe^{II}Pc (top). (b) Ex situ Fe K-edge XANES spectra of CNT/PC, control samples, and references. (c) XANES spectrum of CNT/PC and its linear combination fit from XANES spectra of Fe^{II}Pc and Fe foil.

absorption spectroscopy (XAS) suggested that interaction of the silica layers with the Fe−N_4 moieties protects the Fe−N_4 sites and prevents the formation of large Fe-based particles. The final CNT/PC catalyst comprised relatively high density of Fe−N_x sites, as revealed by XAS analysis combined with atomic-resolution transmission electron microscopy (AR-TEM) and Mössbauer spectroscopy. The CNT/PC catalysts showed very high ORR activity in alkaline media with a half-wave potential of 0.88 V (vs reversible hydrogen electrode, RHE), and they also demonstrated remarkable stability in alkaline media. Importantly, the CNT/PC cathode-based alkaline AEMFC exhibited record high current and power densities among NPMC-based AEMFCs. In addition, the CNT/PC cathode also showed high performance for acidic PEMFCs, with a volumetric current density of 320 A cm^{-3}, which is comparable to the DOE 2020 target (300 A cm^{-3}). Finally, our synthetic strategy was generalized to other carbon supports such as reduced graphene oxides and carbon blacks.

RESULTS AND DISCUSSION

Synthesis and Characterization of CNT/PC Catalysts. Figure 1 illustrates the overall preparation scheme for the CNT/PC catalyst. CNTs were mixed with a porphyrin precursor. The porphyrin-adsorbed CNTs were heated to 400 °C to form CNTs wrapped with porphyrin layers via $\pi-\pi$ interactions. This composite was overcoated with a silica layer. Finally, the ternary composite was subjected to high temperature pyrolysis, followed by etching of the silica layer. The pyrolysis temperature and the ratio of CNT to a porphyrin precursor were controlled to optimize the synthetic conditions. The best-performing catalyst was obtained by 2.0 g 5,10,15,20-tetrakis(4-methoxyphenyl)-21*H*,23*H*-porphine iron(III) chloride (Fe^{III}TMPPCl) per gram of CNTs at the pyrolysis temperature of 800 °C (Figure S1).

TEM images of pristine CNTs (Figure S2) and AR-TEM images of CNT/PC (Figures 2a,b and S3) clearly show the formation of a uniform few-nanometer-thick carbonaceous layer on an individual CNT. The tracking of each synthetic step of CNT/PC by high-angle annular dark-field scanning TEM (HAADF-STEM) combined with elemental mapping images confirmed the formation of the carbon layer after low-temperature heat treatment at 400 °C (Figure S4) and the silica layer after high-temperature pyrolysis at 800 °C (Figure S5). In the final CNT/PC structure, a uniform porphyrinic carbon layer containing iron and nitrogen species can be confirmed (Figure S6). Electron energy loss spectroscopy (EELS) data (Figure 2d) taken from a very small area (the red spot in the HAADF-STEM image in Figure 2c) showed the presence of Fe and N species. The EELS spectrum along with X-ray diffraction (XRD) pattern (Figure S7) of the CNT/PC consistently indicates that Fe species could be dispersed in the carbon layer as subnanometer entities without the formation of large nanoparticles. The Fe and N contents of the CNT/PC were determined to be 0.6 at % (2.9 wt %) and 1.6 at % (1.9 wt %), respectively, by inductively coupled plasma optical emission spectroscopy and combustion elemental analysis. In the Raman spectra (Figure S8), broadening of D band was clearly observed in the CNT/PC compared to the pristine CNTs, indicating the formation of amorphous porphyrinic carbon layer on the surface. Carbon 1s X-ray photoelectron spectroscopy data (Figure S9a) confirmed the relatively amorphous surface of the CNT/PC to that of the pristine CNTs, evidenced by negatively

DOI: 10.1021/jacs.6b09470
J. Am. Chem. Soc. 2016, 138, 15046−15056

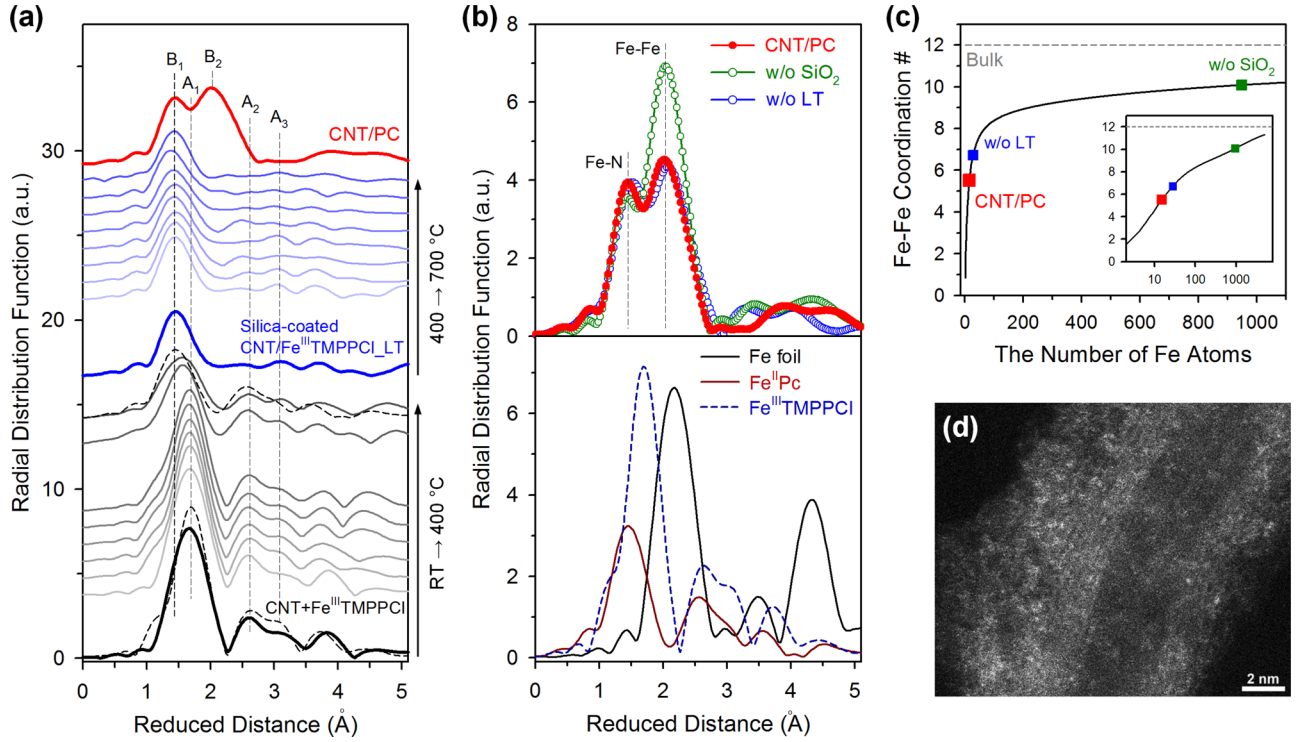

Figure 4. (a) Temperature-dependent RDFs of FT k^3-weighted Fe K-edge EXAFS spectra during two-step pyrolysis of CNT/PC. Those of Fe^{III}TMPPCl (bottom) and Fe^{II}Pc (top) are indicated by the dashed lines. (b) RDFs of FT k^3-weighted Fe K-edge EXAFS spectra of CNT/PC and control samples, and references. (c) Plot for the relation between Fe−Fe coordination number and the number of Fe atoms. The inset of (c) shows the logarithmic representation. (d) HAADF-STEM image of CNT/PC.

shifted carbon−carbon binding energy. In addition, the broad $\pi-\pi^*$ shakeup peak at around 291 eV, which is the characteristic feature of CNT, disappeared for the CNT/PC. From the deconvolution of N 1s XPS spectra, the presence of four types of nitrogen was confirmed (Figure S9b). Raman and XPS data consistently indicate the formation of amorphous porphyrinic carbon layers on the CNT in the CNT/PC as observed in the TEM images.

To clarify the role of silica overcoating step, CNT/PC without silica layers (CNT/PC_w/o SiO_2) was also synthesized. The TEM image of CNT/PC_w/o SiO_2 (Figure S10a) shows that porphyrinic carbon layers were not formed uniformly on the CNTs. Notably, nanoparticles of size up to a few tens of nanometers were formed, as indicated by the TEM image as well as XRD pattern of CNT/PC_w/o SiO_2 (Figure S7). CNT/PC was prepared without low-temperature heat-treatment at 400 °C (CNT/PC_w/o LT) as another control sample. The TEM image of CNT/PC_w/o LT (Figure S10b) indicates an aggregated morphology with nonuniform formation of porphyrinic layers. These control experiments clearly suggest that the silica layer overcoating and the low-temperature annealing step facilitate the formation of uniform porphyrinic carbon layers on individual CNTs, suppressing the formation of large nanoparticles.

X-ray Absorption Spectroscopy. Unraveling the local and electronic structure of catalytically active iron-containing species is critical in establishing a structure−activity relationship of Fe−N/C catalysts. Figure 3a shows temperature-dependent in situ Fe K-edge X-ray absorption near edge structure (XANES) spectra taken under N_2 flow, which revealed the thermally induced structural changes around Fe sites from the precursor mixture to the final CNT/PC. In the initial heat-treatment region (room temperature (RT) to 400 °C), the pre-edge peak feature (peak **A**) shown for precursor mixture of CNT and Fe^{III}TMPPCl (thick black curve) appeared for all spectra below 400 °C, which originates from the square pyramidal symmetry of Fe^{III}TMPPCl precursor (bottom dashed line). A new pre-edge feature (peak **B**) for square planar D_{4h} symmetry appeared at ∼400 °C, indicative of the removal of the axial Cl^- ion from the Fe^{III}TMPPCl (see also the XANES spectrum of iron(II) phthalocyanine (Fe^{II}Pc) shown as top dashed line). After the silica layer coating (shown in thick blue curve), the peak **B** disappeared, implying the formation of an additional axial coordination between silica and the square planar Fe−N_4 site. This suggests that the interaction with the silica protective layer stabilizes the Fe−N_4 site, thereby suppressing the formation of Fe-based nanoparticles during high-temperature pyrolysis. During the pyrolysis to 700 °C, peak **A** underwent a negative shift to peak **A*** and peak **B** appeared again, which are correlated to effective reduction of Fe^{III} to Fe^{II}, and the recovery of the square planar Fe−N_4 site, respectively.

In addition, the temperature-dependent XANES spectra show a noticeable change in the intensity for the peaks **C** (∼7131 eV) and **D** (∼7138 eV). With increased temperature, the intensity of peak **C** gradually increased, whereas that of peak **D** decreased, resulting in an increase in the relative intensity ratio of the peak **C** to peak **D**. Recently, Mukerjee and co-workers demonstrated that an increase in the relative intensity of the peak **C** to peak **D** is attributed to the enhanced distortion of the Fe−N_4 local structure, which can be correlated to the enhancement of ORR activity.[66] On the other hand, Dodelet et al. revealed that Fe−N_{2+2} site with axial N (i.e., D3 site), identified using ^{57}Fe Mössbauer spectroscopy, is

DOI: 10.1021/jacs.6b09470
J. Am. Chem. Soc. 2016, 138, 15046−15056

responsible for high ORR activity.[57] In the D3 site, the Fe atom is off-center with respect to the planar Fe−N_{2+2} approaching the axial N, thus yielding a distorted local structure. On the basis of these results, we suppose that the Fe−N_x site in the CNT/PC transformed gradually into a structure with higher degree of distortion that can boost ORR activity during pyrolysis.

The relative amount of Fe−N_x sites to Fe-based particles in the CNT/PC and CNT/PC_w/o SiO_2 was compared by the linear combination fitting (LCF) of the XANES spectra for these samples, using pure $Fe^{II}Pc$ and Fe metal foil as references (Figures 3b,c). The LCF analysis indicates that the ratio of Fe−N_4 sites to metallic phase Fe is higher for the CNT/PC (73%:27%) than for CNT/PC_w/o SiO_2 (48%:52%). This clearly demonstrates the important role of the silica protective layer in promoting the formation of Fe−N_x sites.

The evolution of local structure was further investigated by extended X-ray absorption fine structure (EXAFS). The radial distribution functions (RDFs) of the EXAFS spectra (Figure 4a) during the heat-treatments suggest that Fe−N_4 sites with axially positioned Cl^- ions (peak **A1**) and ring carbons (peaks **A2** and **A3**) in the precursor mixture are transformed into Fe−N_x sites (peak **B1**) and metallic Fe (peak **B2**) in the final CNT/PC catalyst, consistent with the XANES results. The EXAFS data further confirmed the critical dependence of metallic cluster growth on the silica coating step. The EXAFS spectrum of CNT/PC_w/o SiO_2 shows higher peak intensity for Fe−Fe bonding at around 2.0 Å (Figure 4b) compared to that for the CNT/PC, confirming the TEM observations. On the basis of the well-known relationship between coordination number and particle size (or the number of atoms) in the EXAFS spectra, the number of Fe atoms present as metallic Fe in the CNT/PC was estimated to be ∼10 corresponding to few-angstroms in size, whereas the CNT/PC_w/o SiO_2 contained on average 1000 Fe atoms in each Fe particles (Figure 4c). The very small Fe clusters in the CNT/PC could be directly observed with the HAADF-STEM images (Figures 4d and S6), which show subnanometer particles corresponding to a few Fe atoms or even to monatomic dispersion of the Fe site (perhaps Fe−N_x).

^{57}Fe Mössbauer Spectroscopy. To gain deeper insight into the structure of Fe-related species in CNT/PC and CNT/PC_w/o SiO_2 catalysts pyrolyzed at 800 °C, ^{57}Fe Mössbauer spectroscopy was carried out at 295 K (Figure 5). The Mössbauer spectra were least-squares fitted with subspectra. It is clear that the Mössbauer spectrum of CNT/PC shows greater areas for doublet peaks (D1, D2, and D3), which are assigned to Fe−N_4 species, compared to that of CNT/PC_w/o SiO_2. In contrast, the CNT/PC_w/o SiO_2 exhibits a higher proportion of singlet (Sing) and sextet (Sext1 and Sext2) peaks than the CNT/PC, indicating the formation of larger amount of less active Fe and Fe_3C phases in CNT/PC_w/o SiO_2. The Fe-site assignment, corresponding fitting parameters, and the relative peak area for the catalysts are summarized in Table S1.

Mössbauer spectroscopy analysis over our catalysts indicates that the silica coating is effective to preserve Fe−N_4 species and to suppress the formation of Fe-based particles. Relative absorption areas for all doublets of CNT/PC are larger than that of CNT/PC_w/o SiO_2 (76% and 49% of Fe−N_4 species with and without silica coating, respectively). 24% of Fe and Fe_3C species in CNT/PC are attributed to the presence of subnanometer-sized Fe clusters, while tens-of-nanometer-sized Fe and Fe_3C nanoparticles (accounting for 51%) are included

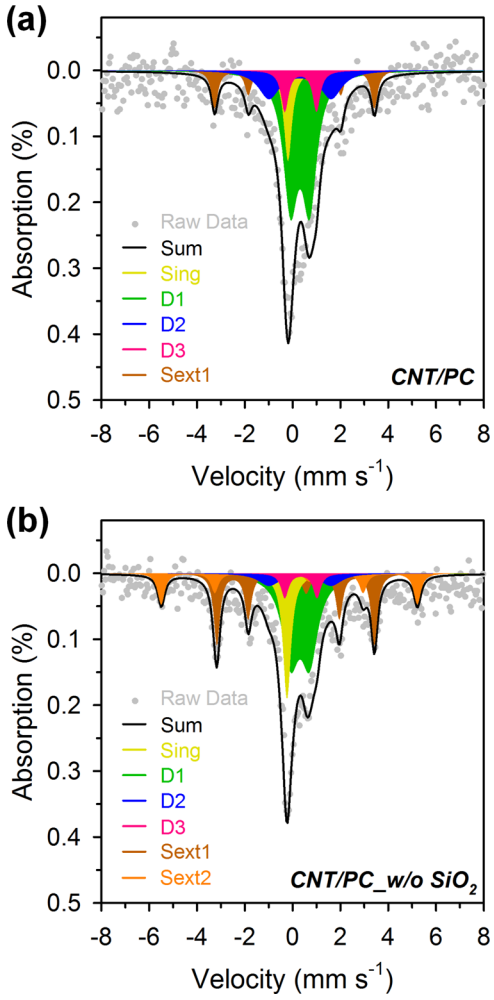

Figure 5. ^{57}Fe Mössbauer spectra for (a) CNT/PC and (b) CNT/PC_w/o SiO_2 catalysts pyrolyzed at 800 °C.

in CNT/PC_w/o SiO_2. The Mössbauer spectroscopy results are consistent with XRD, TEM, and XAS analyses.

Half-Cell Rotating Ring Disk Electrode Test. The ORR activities of the CNT/PC and a Pt/C catalyst (20 wt % Pt, Johnson-Matthey) were evaluated using rotating ring-disk electrode (RRDE) measurements in both alkaline and acidic media (Figure 6a). The linear sweep voltammetry (LSV) curve of CNT/PC in 0.1 M KOH (Figure 6a) clearly demonstrates the very high ORR activity of CNT/PC in alkaline electrolyte, with the half-wave potential at 0.88 V, which compares favorably to Pt/C. Moreover, the number of transferred electrons during the ORR was close to four in the entire potential region, indicating near-four-electron selectivity in alkaline media (Figure S11 and See Supporting Text). We also measured the ORR activities of CNT/PC_w/o SiO_2 and CNT/PC_w/o LT (Figure 6c), which are less pronounced compared to that of CNT/PC, as indicated by the lower on-set and half-wave potentials (Table S2). These results confirm the critical role of the silica protective layer as well as low-temperature annealing step for enhancing ORR activity. A comparison of the alkaline ORR activity of CNT/PC with previously reported M−N/C catalysts (Table S3) revealed that CNT/PC is among the best performing ORR catalysts. We note that, however, differing experimental conditions such as catalyst loading among different catalysts can potentially

DOI: 10.1021/jacs.6b09470
J. Am. Chem. Soc. 2016, 138, 15046−15056

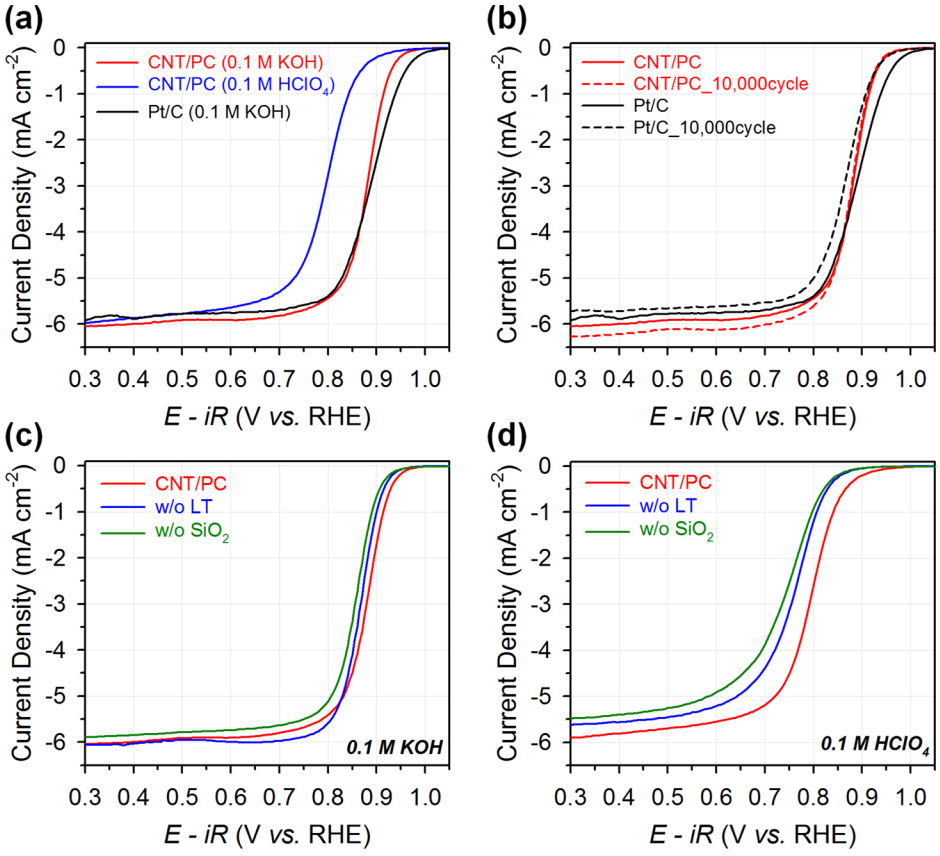

Figure 6. Polarization curves for the ORR activity of (a) CNT/PC and Pt/C, (b) CNT/PC and Pt/C before and after 10 000 potential cycles in 0.1 M KOH. (c,d) ORR activity comparison between CNT/PC and control samples in (c) 0.1 M KOH and (d) 0.1 M $HClO_4$. The measurements were conducted with the electrode rotation of 1600 rpm.

influence the ORR activity. The long-term durability of the CNT/PC catalyst, measured by cycling the potential between 0.6 and 1.0 V up to 10 000 times, was remarkably high with a nearly identical LSV curve after 10 000 cycles, whereas Pt/C underwent a significant decrease in its catalytic activity with a negative shift of its half-wave potential by 25 mV (Figure 6b).

The CNT/PC also shows high ORR activity in acidic media (Figure 6a). The LSV curve of CNT/PC for the ORR in 0.1 M $HClO_4$ reveals a half-wave potential at 0.79 V (Table S4). The ORR activity of CNT/PC in acidic media was also compared with reported catalysts. The kinetic parameters of CNT/PC are higher than most of the catalysts reported in the literature (Table S5). Its ORR activity in terms of half-wave potential is comparable to the best M−N/C catalysts to date. The CNT/PC catalyst also outperformed the control catalysts (CNT/PC_w/o SiO_2 and CNT/PC_w/o LT; Figure 6d) in acidic media. Interestingly, the effectiveness of the silica-protective strategy appeared to be more prominent in acidic media. The difference in the activities of CNT/PC and CNT/PC_w/o SiO_2 was larger in acidic media. Further investigations into the possibility of a different ORR mechanism on Fe−N_x sites with the pH of electrolyte are needed.[60,61]

Calculation of Turnover Frequency. Turnover frequencies (TOFs), representing an intrinsic activity per each active site, of our catalysts were calculated at 0.8 and 0.9 V (vs RHE) for the ORR in acidic and alkaline media, respectively (See calculation details in the Supporting Information). For the calculation of TOF for Fe−N/C catalysts, detailed understanding of Fe-containing active sites is important. Mössbauer spectroscopy analysis revealed that the three doublets, D1−D3, correspond to three structurally distinctive Fe−N_4 sites.[35,56,74] D1 is assigned to in-plain low-spin (S = 0) ferrous Fe−N_4 site. Koslowski et al.[56] revealed that D1 site is responsible for 4-electron ORR in 0.5 M H_2SO_4. Since then, the in-plane D1 has been considered as the active site for the ORR in acidic media. D2 is crystalline-FePc-like Fe−N_4 site with pseudo-octahedral coordination with axial N atoms from the adjacent FePc. This coordination environment and fully occupied d_{z2} orbital of Fe center in D2 render the adsorption of O_2 on this site unfavorable, suggesting negligible contribution of the site to the ORR activity.[35,56,57,74] D3, porphyrin-like Fe−N_4 site with intermediate-spin, is proposed to exist through the stabilization from carbon frameworks.[35] However, in-depth investigation of D3 site and its relation to the ORR activity has not been discussed yet. On the basis of these considerations on each doublet site, we decided to use the D1 as the active site for the acidic ORR. In acidic media, the TOF of CNT/PC was calculated to be 0.22 e $site^{-1}$ s^{-1}, which is in the range of similar activity to previous works.[35,56,65] For the ORR in alkaline media, there has been no report that clearly reveals which Fe−N_4 species is responsible for the ORR. Hence, TOFs were calculated by considering only D1 site or all doublet sites as the active center, which yield 2.6 and 1.7 e $site^{-1}$ s^{-1}, respectively. It is noteworthy that the difference in the TOFs between the CNT/PC and CNT/PC_w/o SiO_2 is significant; the CNT/PC shows 300% and 40−50% higher TOF in acidic and alkaline media, respectively. The higher intrinsic activity of an individual active site in the sample with silica coating may suggest

DOI: 10.1021/jacs.6b09470
J. Am. Chem. Soc. 2016, 138, 15046−15056

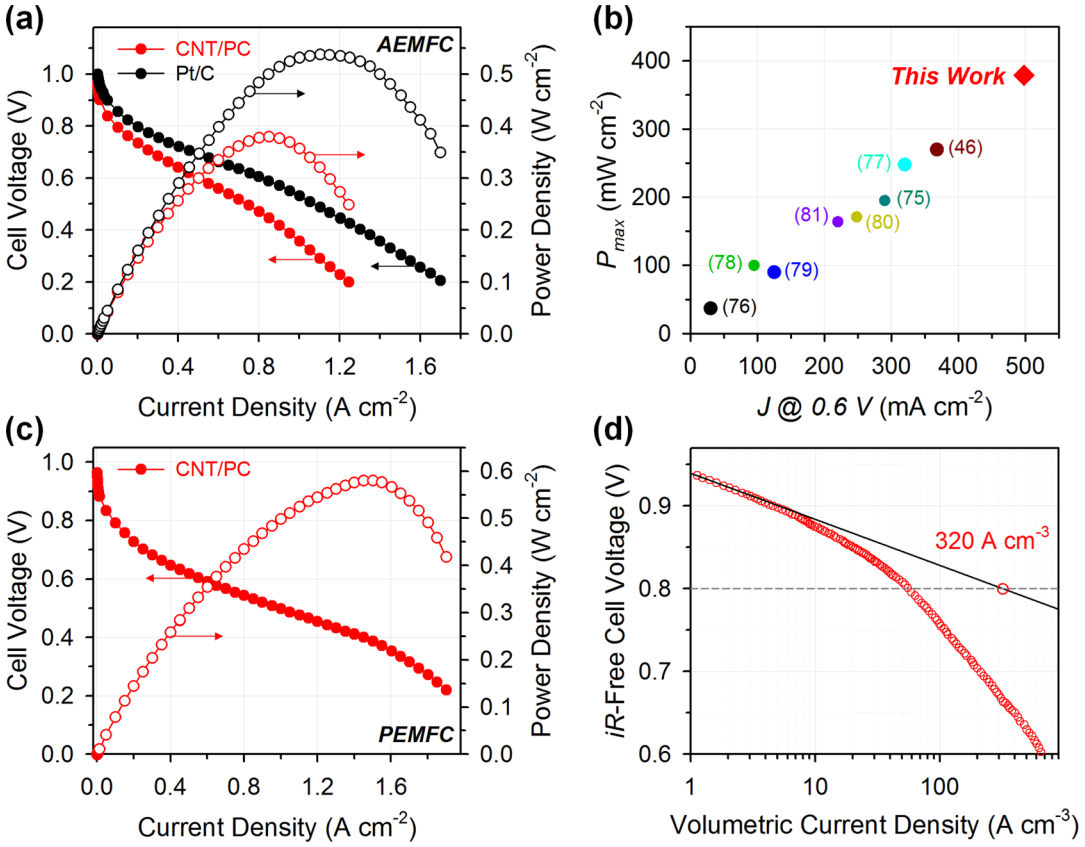

Figure 7. Single cell performances. (a) Alkaline AEMFC performances of MEAs using CNT/PC and Pt/C as cathode catalysts. (b) Comparison of current density at 0.6 V and peak power density of CNT/PC-based AEMFC with those of previously reported AEMFCs based on NPMC-based MEAs. The numbers in the brackets denote the reference numbers. (c) Acidic PEMFC performance of CNT/PC-based MEA. (d) Volumetric current densities of the CNT/PC in the PEMFC. Detailed experimental conditions are presented in the Supporting Information.

implications about the role of the silica in promoting the activity of Fe−N_x sites.

Single-Cell Tests for AEMFC and PEMFC. We exploited the CNT/PC catalyst as a cathode for an AEMFC. Figure 7a shows polarization and power density curves of AEMFCs based on CNT/PC and Pt/C catalysts. The CNT/PC-based membrane electrode assembly (MEA) exhibited very high AEMFC performance, which was comparable to a Pt/C-based MEA. The current density at 0.6 V and peak power density of the CNT/PC-based MEA are 498 mA cm^{-2} and 0.38 W cm^{-2}, respectively, which are record high performances among NPMC-based MEAs for AEMFCs (Figure 7b and Table S6).[46,75−81] High performance of a CNT/PC-based MEA was also demonstrated in a PEMFC (Figures 6c and 6d). The CNT/PC-based MEA exhibited a current density at 0.6 V and peak power density of 550 mA cm^{-2} and 0.58 W cm^{-2}, respectively. Significantly, the volumetric current density of the CNT/PC-based MEA in the PEMFC is 320 A cm^{-3}, which compares favorably with the US Department of Energy 2020 target (300 A cm^{-3}) and exceeds the reported values of the majority of previous catalysts (Table S7). The excellent single cell performances indicate that the high ORR activity of the CNT/PC catalyst significantly enhances the MEA performances in both alkaline and acidic electrolytes.

Role of the Silica Coating. To more clearly establish the role of silica coating layer on the composition, coordination environment, and ORR activity of CNT/PC-based catalysts, a set of CNT/PC samples with and without silica layer were prepared at various pyrolysis temperatures from 600 to 1000 °C (denoted as CNT/PC-X and CNT/PC-X_w/o SiO_2, X = temperature). First, combustion elemental analysis was used to determine nitrogen contents in the samples (Table S8). CNT/PC has a larger amount of nitrogen than CNT/PC_w/o SiO_2 for the samples pyrolyzed at 600 and 700 °C. However, when the samples were heat-treated at higher than 800 °C, the nitrogen contents of CNT/PC and CNT/PC_w/o SiO_2 are almost similar to each other. These results indicate that the silica coating does not always make the samples richer in nitrogen atoms. It is noted that nitrogen species can exist as at least three forms after pyrolysis and acid washing. (i) Nitrogen remains coordinated to Fe to form Fe−N_x species. (ii) Nitrogen can be incorporated within graphitic carbon shells encapsulating Fe (and/or Fe_3C) particles produced during pyrolysis at higher temperature (≥800 °C). (iii) Nitrogen species without Fe-coordination can be generated during the acid washing step, which can remove Fe from unstable Fe−N_x species. Hence, the nitrogen contents may not be directly correlated to the amount of Fe−N_x species.

X-ray photoelectron spectroscopy (XPS) was conducted to gain further insight into nitrogen species in the samples. N 1s XPS spectra are presented in Figure S12 with four deconvoluted peaks: 398.1−398.3 eV for pyridinic N (N1), 399.4 eV for pyrrolic N and Fe−N_x species (N2), 400.4−400.7 eV for graphitic N (N3), and >402 eV for N−O species (N4).[26,67,82] The most notable difference in the XPS spectra is larger relative peak area of N2 peak (pyrrolic N and Fe−N_x) for the silica-coated samples, regardless of pyrolysis temperature. This suggests that the silica coating effectively preserve Fe−N_x

DOI: 10.1021/jacs.6b09470
J. Am. Chem. Soc. 2016, 138, 15046−15056

species yielding the Fe−N/C catalyst with a higher density of Fe−N_x sites. Another notable point from XPS analysis is relatively larger N3 peak area (graphitic N) for CNT/PC_w/o SiO_2 samples pyrolyzed at higher temperatures (≥800 °C). As described above, high-temperature pyrolysis of Fe−N−C precursor usually produces Fe (and/or Fe_3C) particles, which are encapsulated by graphitic carbon shells. The larger N3 peak area in CNT/PC_w/o SiO_2 samples suggests that higher amount of nitrogen could be incorporated within graphitic shells in these samples than silica coated ones.

We accessed the structure of prepared samples by XRD. CNT/PC samples prepared with the silica overcoating layer showed no characteristic XRD peaks for Fe and Fe_3C (Figure S13). In contrast, CNT/PC_w/o SiO_2 samples pyrolyzed at 700−1000 °C contained Fe and Fe_3C nanoparticles. The formation of the Fe and Fe_3C particles were particularly prominent for CNT/PC-900_w/o SiO_2 and CNT/PC-1000_w/o SiO_2. We highlight that the silica coating strategy is efficient in suppressing Fe-based particle formation at high temperature up to 1000 °C.

Finally, we investigated the electrocatalytic activity of the prepared catalysts for the ORR in both alkaline and acidic media. The results indicate that the silica coating is generally effective to enhance the ORR activity of the samples in both electrolytes (Figures S14 and S15). In all pyrolysis temperature range investigated, CNT/PC exhibited 20−60 mV and 50−70 mV positive half-wave potentials than CNT/PC_w/o SiO_2 in 0.1 M KOH and 0.1 M $HClO_4$, respectively. Interestingly, the CNT/PC-600 exhibited about 2−3 times higher ORR activity than CNT/PC-600_w/o SiO_2 although both samples do not have Fe-based large particles. XPS results suggest that the CNT/PC-600 contains a larger amount of Fe−N_x species by 30% than CNT/PC-600_w/o SiO_2, which however cannot explain fully the improvement factor. Kramm et al.[83] reported Fe−N/C catalysts based on pyrolyzed Fe^{III}TMPPCl. In that work, Mössbauer spectra of Fe^{III}TMPPCl heat-treated at 600 °C showed that Fe-sites in the catalyst are mostly composed of Fe−N_4 site. However, it showed inferior ORR activity to the catalyst pyrolyzed at 800 °C, which had smaller amount of active Fe−N_4 species. The literature highlights the importance of the electron density as well as the site density of the Fe−N_4 center.[83] In our work, we suppose that the silica coating plays a role not only in preserving active Fe−N_x site, but also in modulating the electronic structure (and/or local structure) of the Fe−N_x site via interaction between the silica and Fe−N_4 in the precursor. The modulation may be related to the distortion of Fe−N_x site.[66]

Generalization of the Synthetic Strategy to Other Carbon Supports. To validate the generality of this approach, we extended the silica-protected-layer-assisted strategy to other carbon supports, i.e., reduced graphene oxides (rGO), Ketjen black (KB), acetylene black (AB), Vulcan; the resulting catalysts were denoted as carbon/PC (carbon: rGO, KB, AB, Vulcan). The XRD patterns of the rGO/PC and KB/PC catalysts show only graphitic carbon-like peaks, whereas the rGO/PC_w/o SiO_2 and KB/PC_w/o SiO_2 show additional diffraction peaks, corresponding to Fe_3C and metallic Fe, bolstering the role of silica overcoating layer in suppressing the formation of Fe-based particles during pyrolysis (Figure 8a). Relatively higher density of active Fe−N_x species in the carbon/PC catalysts resulted in greater ORR activity (Figure 8b). The XRD patterns and ORR activity data for AB/PC and Vulcan/PC catalysts (Figure S16) also demonstrate the advantage of this strategy to preferentially create Fe−N_x sites, resulting in enhanced ORR activity. Hence, the silica-protective-layer-assisted synthetic method is extensively applicable to other carbon supports for developing pyrolyzed M−N/C catalyst with higher density of active M−N_x sites.

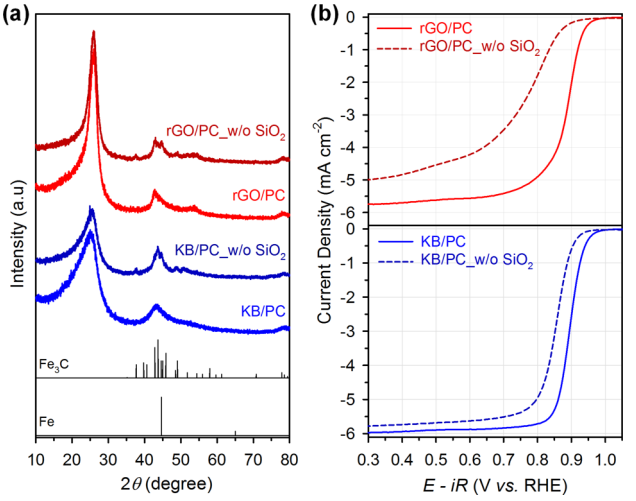

Figure 8. (a) XRD patterns for rGO/PC, rGO/PC_w/o SiO_2, KB/PC, and KB/PC_w/o SiO_2. (b) Comparison of ORR activity of rGO/PC and rGO/PC_w/o SiO_2, and KB/PC and KB/PC_w/o SiO_2 in 0.1 M KOH at the electrode rotation speed of 1600 rpm.

Catalytic Role of Fe−N_x and Fe-Based Particles in ORR. In order to identify the catalytic role of the Fe−N_x site and Fe-based particles for the ORR, we performed electrochemical in situ Fe K-edge XAS over CNT/PC catalyst. In situ XAS analysis revealed that the ORR over CNT/PC catalyst proceeds predominantly via direct participation of the Fe−N_x sites (Figure S17 and See Supporting Text). It should be noted that, recently, iron and iron carbide particles have also been suggested as possible active species, along with Fe−N_x sites,[18,19,27,31,68] although their roles are still controversial. Bao et al. reported that Fe nanoparticles encapsulated in CNTs modify the electronic structure of the carbons, and thus indirectly participate in the ORR electrocatalysis.[19] In addition, it has been suggested that the ORR activity of Fe−N_x sites can be boosted by adjacent Fe_3C particle.[68] In our study, the carbon/PC catalysts with a relatively higher density of Fe−N_x sites showed better ORR activity than carbon/PC_w/o SiO_2 catalysts. The abundance of Fe−N_x sites is responsible for the higher ORR activity of the carbon/PC, and therefore they are regarded as the main active site for the ORR. However, the four-electron selectivity of the carbon/PC_w/o SiO_2 catalysts were slightly, yet consistently, higher than the carbon/PC catalysts in the diffusion-limited potential region, in spite of lower ORR activity of the former than the latter (Figure S18). These results suggest that the Fe-based particles present in the carbon/PC_w/o SiO_2 catalysts reduce HO_2^-, which is the product of 2-electron ORR, completing the 4-electron reduction of oxygen.

CONCLUSION

We have demonstrated a universal silica-protective-layer-assisted strategy to preferentially create catalytically active Fe−N_x sites during the preparation of Fe−N/C catalysts. Temperature-controlled in situ XAS provided evidence for the possible role of the silica layer in promoting the formation of

DOI: 10.1021/jacs.6b09470
J. Am. Chem. Soc. 2016, 138, 15046−15056

Fe−N_x sites, while suppressing the formation of Fe-based particles, as well as for the distortion of the planar Fe−N_4 site to more active distorted Fe−N_x site. The resulting highly active nonprecious metal ORR catalyst, CNT/PC, showed very high ORR activity in both alkaline and acidic media, and demonstrated excellent fuel cell performances in both an AEMFC and a PEMFC. Significantly, the AEMFC with a CNT/PC cathode showed record high current and power densities among NPMC-based MEAs. We further demonstrated the general applicability of the synthetic strategy with respect to other carbon supports including rGO and carbon blacks. This work indicates that the "silica-protective-layer-assisted" strategy can be exploited to promote the formation of active molecular entity (Fe−N_x sites) during the catalyst synthesis, beyond the previous role of preventing the sintering of nanoparticle catalysts under harsh catalytic reaction conditions. We believe that our catalyst design can provide an important guideline for the development of novel M−N/C catalysts that can be applied to a wide range of energy conversion and storage devices.

EXPERIMENTAL METHODS

Synthesis of CNT/PC Catalysts. Fe^{III}TMPPCl was purchased from Porphyrin Systems. Tetraethyl orthosilicate (TEOS) and formic acid were purchased from Aldrich. All chemicals were used as received. Multiwalled carbon nanotubes (CNTs, < 10 nm in diameter, 5−15 mm in length) were purchased from Carbon Nanomaterial Technology Co., Ltd. In order to remove metal impurities, the CNTs were treated with nitric acid (63%) for 12 h at 80 °C and subsequently with hydrochloric acid (37%) for 12 h at 80 °C.

For the optimized preparation of CNT/PC, CNTs (100 mg) were mixed with Fe^{III}TMPPCl (200 mg) in an agate mortar for 5 min. The mixture was heated from room temperature (RT) to 400 °C in a quartz-tube furnace at a ramping rate of 2 °C min^{-1} and maintained at that temperature for 3 h under N_2 gas (99.999%) at a flow rate of 1 L min^{-1}. The heat-treated CNT/Fe^{III}TMPPCl composite was mixed with 0.5 mL of TEOS in a mortar, followed by mixing with 0.5 mL of formic acid. The CNT-Fe^{III}TMPPCl-silica composite was placed in an alumina crucible and dried in a 60 °C oven for 3 h. The composite was then heated to 800 °C at a ramping rate of 2 °C min^{-1} and maintained at that temperature for 3 h under N_2 gas at a flow rate of 1 L min^{-1}. The resulting CNT/PC-silica composite was mixed with 2:1 (v/v) = ethanol:10% aqueous HF solution and stirred for 30 min to etch the silica, followed by filtering and washing with ethanol several times. The HF etching process was repeated in the same manner, and the resulting sample was dried at 60 °C to afford CNT/PC samples. CNT/PC_w/o SiO_2 and CNT/PC_w/o LT were prepared in the same manner as described above, except the omission of TEOS/formic acid addition and heat-treatment at 400 °C, respectively.

Physical Characterization. X-ray diffraction (XRD) patterns of the samples were obtained using an X-ray diffractometer (Rigaku D/Max 2500 V/PC) equipped with a Cu Kα source operating at 40 kV and 200 mA. High resolution transmission electron microscopy (HR-TEM) images were obtained using a JEOL JEM-2100 microscope. High-angle annular dark-field scanning transmission electron microscopy (HAADF STEM) images and the corresponding elemental mapping images were obtained using a JEOL JEM-2100F microscope with a probe-forming Cs corrector at 200 kV. Atomic resolution structures of the samples were observed using an image-side spherical aberration corrected transmission electron microscope (TEM, Titan3 G2 cube 60−300, FEI Company, Netherlands) under an accelerating voltage of 80 keV. X-ray photoelectron spectroscopy (XPS) measurements were performed on an ESCLAB 250Xi (Thermo Scientific), equipped with a monochromatic Al Kα X-ray source (1486.6 eV). Individual chemical components of the N 1s binding energy region were fitted to the spectra using the mixed (Gaussian 70, Lorentzian 30)-function after a Shirley-type background subtraction. The Raman spectra were obtained using a WITec alpha300R coupled with a He−Ne laser of 532 nm at 1.0 mW. Fe contents in the catalysts were characterized using inductively coupled plasma optical emission spectrometer (700-ES, Varian). Combustion analysis was conducted using an elemental analyzer (Flash 2000, ThermoFisher Scientific) to determine the contents of C, N, H, and O in the catalysts.

X-ray Absorption Spectroscopy. X-ray absorption spectroscopy (XAS) was performed at the beamline 6D and 10C of the Pohang Accelerator Laboratory (PAL). The incident X-ray had the electron beam energy and current of 3.0 GeV and 300 mA, respectively. A Si(1 1 1) double crystal monochromator was used to filter the incident photon energy, which was detuned by 30% to remove high-order harmonics. Ex situ Fe K-edge XAS experiments were performed with pelletized samples in both transmission and fluorescence detection modes.

For temperature-dependent in situ Fe K-edge XAS, a mixture of CNT and Fe^{III}TMPPCl and silica-coated CNT/PC after low-temperature (400 °C) treatment were ground in an agate mortar, pressed into pellets of 16 mm in diameter, and fixed in a heating chamber under nitrogen gas flow. For the CNT and Fe^{III}TMPPCl mixture, the temperature was raised from RT to 400 °C, during which total eight XAS spectra were obtained. For the silica-coated CNT/PC after low-temperature treatment, the temperature was rapidly increased to 400 °C, and gradually raised to 700 °C, during which eight XAS spectra were taken.

For electrochemical in situ XAS, a CNT/PC catalyst ink (described in the following section) was deposited onto a piece of carbon paper, and heat-pressed. The catalyst-coated carbon paper was attached to a homemade spectroelectrochemical cell, with the catalyst layer in contact with 0.1 M KOH. Then, Fe K-edge XAS spectra were obtained without applied potential, and subsequently under potentials of 0.3 V. and 0.9 V (vs RHE, *iR*-corrected) in fluorescence detection mode.

Mössbauer Spectroscopy. The Mössbauer spectra were recorded in transmission mode with a ^{57}Co source in a rhodium matrix. The Mössbauer spectrometer of the electromechanical type was fixed absorber and operated source on constant-acceleration mode, which was calibrated by using an α-Fe foil. Mössbauer spectra were least-squares fitted, providing the values of hyperfine field (H_{hf}), isomer shift (δ_{iso}), electric quadrupole splitting (ΔE_Q), and relative area of Fe ions.[84]

Electrochemical Characterization. Electrochemical experiments were performed with a bipotentiostat (CHI760E, CH Instruments) and rotator (AFMSRCE, Pine Research Instrumentation) at RT (25 °C) using a three-electrode electrochemical cell. Hg/HgO (CHI152, CH Instruments; 1 M KOH filling solution) and Ag/AgCl (RE-1B, ALS; saturated KCl filling solution) reference electrodes were used for measurements in alkaline and acidic media, respectively, and a graphite rod was used as the counter electrode. A rotating ring-disk electrode (RRDE, AFE7R9GCPT, Pine Research Instrumentation) was used as the working electrode. Prior to every measurement, the RRDE was polished with a 1.0 μm alumina suspension and then with a 0.3 μm suspension to afford a mirror finish. To prepare the catalyst ink, the catalyst (30 mg) was mixed with deionized (DI) water (0.1 mL), ethanol (1.01 mL), and Nafion (0.075 mL, 5 wt % in isopropanol, Aldrich), and the resulting slurry was ultrasonicated for 30 min. For the benchmark Pt/C catalyst (20 wt % Pt, HiSPEC-3000, Johnson-Matthey), a catalyst ink was prepared with the Pt/C catalyst (3.5 mg), DI water (0.1 mL), ethanol (1.07 mL), and Nafion (0.03 mL). The catalyst ink (8 μL of for the CNT/PC, 6 μL for Pt/C) was pipetted with a micropipette onto the glassy carbon disk (0.247 cm^2) of the RRDE, resulting in a catalyst loading of 800 $\mu g\ cm^{-2}$ (14 $\mu g_{Pt}\ cm^{-2}$ for Pt/C). 0.1 M $HClO_4$ (70% Veritas double distilled, GFS Chemicals) and 0.1 M KOH (99.99%, Aldrich) were used as the alkaline and acidic electrolytes, respectively. Before the electrochemical measurements, the catalyst was cleaned by cycling the potential between 0.05 and 1.2 V (vs RHE) for 50 cycles at a scan rate of 100 mV s^{-1} (500 mV s^{-1} for Pt/C) in an N_2-saturated electrolyte. Subsequently, cyclic voltammetry (CV) was performed in the potential range of 0.05 to 1.2 V at a scan rate of 20 mV s^{-1} (50 mV s^{-1} for Pt/C). Linear sweep voltammetry (LSV) polarization curves for the oxygen reduction reaction (ORR)

DOI: 10.1021/jacs.6b09470
J. Am. Chem. Soc. 2016, 138, 15046−15056

were obtained by sweeping the potential from 1.2 to 0.2 V (from −0.01 to 1.1 V for Pt/C) in an O_2-saturated electrolyte with O_2 purging at a rotating speed of 1600 rpm. In order to correct the non-Faradaic current (capacitive current) from the LSV curve, the same measurement was conducted in N_2-saturated electrolyte. To measure solution resistance for *iR*-compensation, electrochemical impedance spectra were obtained at 0.68 V with AC potential amplitude of 10 mV from 10 000 to 1 Hz. For CNT/PC and the control samples, ORR measurements were independently repeated at least three times and the average data were presented.

Calibration of Electrodes with Respect to the Reversible Hydrogen Electrode. The Hg/HgO and Ag/AgCl reference electrodes were calibrated with respect to the reversible hydrogen electrode (RHE) before use. For this purpose, a two-electrode electrochemical cell was built in which a Pt coil and the reference electrode to be calibrated were connected. Ultrapure hydrogen gas was then sparged into the electrolyte. In this case, H^+/H_2 equilibrium was established on the Pt coil, which thus acted as a RHE. A stable open circuit voltage could be observed within several minutes, which was taken to be the conversion value. The calibration values were $E(\text{RHE}) = E(\text{Hg/HgO}) + 0.89$ V and $E(\text{RHE}) = E(\text{Ag/AgCl}) + 0.26$ V in 0.1 M KOH and 0.1 M $HClO_4$, respectively.

■ ASSOCIATED CONTENT

Supporting Information

The Supporting Information is available free of charge on the ACS Publications website at DOI: 10.1021/jacs.6b09470.

Additional experimental information and data (PDF)

■ AUTHOR INFORMATION

Corresponding Authors

*cskim@kookmin.ac.kr
*mgkim@postech.ac.kr
*kty@kier.re.kr
*shjoo@unist.ac.kr

Notes

The authors declare no competing financial interest.

■ ACKNOWLEDGMENTS

This work was supported by the National Research Foundation (NRF) of Korea grant funded by the Ministry of Science, ICT and Future Planning (MISP) (NRF-2015M1A2A2056560) and the KEIT funded by the Ministry of Trade, Industry and Energy (10050509). C.S.K. and J.T.L. were supported by Mid-career Researcher Program through the NRF of Korea grant funded by the MISP (NRF-2014R1A2A1A05002488). Y.J.S. acknowledges the Global Ph.D. Fellowship (NRF-2013H1A2A1032644). The XAS experiments performed at Beamline 6D and Beamline 10C of the Pohang Accelerator Laboratory (PAL) were supported in part by the Ministry of Education, Pohang University of Science of Technology (POSTECH) and UCRF at UNIST.

■ REFERENCES

(1) Steele, B. C. H.; Heinzel, A. *Nature* **2001**, *414*, 345.
(2) Gasteiger, H. A.; Kocha, S. S.; Sompalli, B.; Wagner, F. T. *Appl. Catal., B* **2005**, *56*, 9.
(3) Debe, M. K. *Nature* **2012**, *486*, 43.
(4) Shao, M.; Chang, Q.; Dodelet, J.-P.; Chenitz, R. *Chem. Rev.* **2016**, *116*, 3594.
(5) Xia, W.; Mahmood, A.; Liang, Z.; Zou, R.; Guo, S. *Angew. Chem., Int. Ed.* **2016**, *55*, 2650.
(6) Mistry, H.; Varela, A. S.; Kühl, S.; Strasser, P.; Cuenya, B. R. *Nat. Rev. Mater.* **2016**, *1*, 16009.
(7) Lee, K.; Zhang, J.; Wang, H.; Wilkinson, D. P. *J. Appl. Electrochem.* **2006**, *36*, 507.
(8) Papageorgopoulos, D. U.S. DOE Hydrogen and Fuel Cells Program 2015 Annual Review Meeting, 2015, https://www.hydrogen.energy.gov/pdfs/review15/fc000_papageorgopoulos_2015_o.pdf (accessed Nov 2, 2015).
(9) Jiang, R.; Chu, D. Electrocatalysts for Alkaline Polymer Exchange Membrane (PEM) Fuel Cells—Overview. In *Non-Noble Metal Fuel Cell Catalysts*; Chen, Z., Dodelet, J.-P., Zhang, J., Eds.; Wiley-VCH: Weinheim, 2014; pp 271−317.
(10) Gu, S.; Xu, B.; Yan, Y. *Annu. Rev. Chem. Biomol. Eng.* **2014**, *5*, 429.
(11) Jaouen, F.; Proietti, E.; Lefèvre, M.; Chenitz, R.; Dodelet, J.-P.; Wu, G.; Chung, H. T.; Johnston, C. M.; Zelenay, P. *Energy Environ. Sci.* **2011**, *4*, 114.
(12) Chen, Z.; Higgins, D.; Yu, A.; Zhang, L.; Zhang, J. *Energy Environ. Sci.* **2011**, *4*, 3167.
(13) Lefèvre, M.; Proietti, E.; Jaouen, F.; Dodelet, J.-P. *Science* **2009**, *324*, 71.
(14) Wu, G.; More, K. L.; Johnston, C. M.; Zelenay, P. *Science* **2011**, *332*, 443.
(15) Proietti, E.; Jaouen, F.; Lefèvre, M.; Larouche, N.; Tian, J.; Herranz, J.; Dodelet, J.-P. *Nat. Commun.* **2011**, *2*, 416.
(16) Li, Y.; Zhou, W.; Wang, H.; Xie, L.; Liang, Y.; Wei, F.; Idrobo, J.-C.; Pennycook, S. J.; Dai, H. *Nat. Nanotechnol.* **2012**, *7*, 394.
(17) Zhao, Y.; Watanabe, K.; Hashimoto, K. *J. Am. Chem. Soc.* **2012**, *134*, 19528.
(18) Chung, H. T.; Won, J. H.; Zelenay, P. *Nat. Commun.* **2013**, *4*, 1922.
(19) Deng, D.; Yu, L.; Chen, X.; Wang, G.; Jin, L.; Pan, X.; Deng, J.; Sun, G.; Bao, X. *Angew. Chem., Int. Ed.* **2013**, *52*, 371.
(20) Cao, R.; Thapa, R.; Kim, H.; Xu, X.; Kim, M. G.; Li, Q.; Park, N.; Liu, M.; Cho, J. *Nat. Commun.* **2013**, *4*, 2076.
(21) Cheon, J. Y.; Kim, T.; Choi, Y.; Jeong, H. Y.; Kim, M. G.; Sa, Y. J.; Kim, J.; Lee, Z.; Yang, T.-H.; Kwon, K.; Terasaki, O.; Park, G.-G.; Adzic, R. R.; Joo, S. H. *Sci. Rep.* **2013**, *3*, 2715.
(22) Yuan, S.; Shui, J.-L.; Grabstanowicz, L.; Chen, C.; Commet, S.; Reprogle, B.; Xu, T.; Yu, L.; Liu, D.-J. *Angew. Chem., Int. Ed.* **2013**, *52*, 8349.
(23) Lin, L.; Zhu, Q.; Xu, A.-W. *J. Am. Chem. Soc.* **2014**, *136*, 11027.
(24) Sahraie, N. R.; Paraknowitsch, J. P.; Göbel, C.; Thomas, A.; Strasser, P. *J. Am. Chem. Soc.* **2014**, *136*, 14486.
(25) Liang, J.; Zhou, R. F.; Chen, X. M.; Tang, Y. H.; Qiao, S. Z. *Adv. Mater.* **2014**, *26*, 6074.
(26) Serov, A.; Artyushkova, K.; Atanassov, P. *Adv. Energy Mater.* **2014**, *4*, 1301735.
(27) Yang, W.; Liu, X.; Yue, X.; Jia, J.; Guo, S. *J. Am. Chem. Soc.* **2015**, *137*, 1436.
(28) Ding, W.; Li, L.; Xiong, K.; Wang, Y.; Li, W.; Nie, Y.; Chen, S.; Qi, X.; Wei, Z. *J. Am. Chem. Soc.* **2015**, *137*, 5414.
(29) Niu, W.; Li, L.; Liu, X.; Wang, N.; Liu, J.; Zhou, W.; Tang, Z.; Chen, S. *J. Am. Chem. Soc.* **2015**, *137*, 5555.
(30) Wang, Y.-C.; Lai, Y.-J.; Song, L.; Zhou, Z.-Y.; Liu, J.-G.; Wang, Q.; Yang, X.-D.; Chen, C.; Shi, W.; Zheng, Y.-P.; Rauf, M.; Sun, S.-G. *Angew. Chem., Int. Ed.* **2015**, *54*, 9907.
(31) Strickland, K.; Miner, E.; Jia, Q.; Tylus, U.; Ramaswamy, N.; Liang, W.; Sougrati, M.-T.; Jaouen, F.; Mukerjee, S. *Nat. Commun.* **2015**, *6*, 7343.
(32) Sahraie, N. R.; Kramm, U. I.; Steinberg, J.; Zhang, Y.; Thomas, A.; Reier, T.; Paraknowitsch, J.-P.; Strasser, P. *Nat. Commun.* **2015**, *6*, 8618.
(33) Shui, J.; Chen, C.; Grabstanowicz, L.; Zhao, D.; Liu, D.-J. *Proc. Natl. Acad. Sci. U. S. A.* **2015**, *112*, 10629.
(34) Cheon, J. Y.; Kim, K.; Sa, Y. J.; Sahgong, S. H.; Hong, Y.; Woo, J.; Yim, S.-D.; Jeong, H. Y.; Kim, Y.; Joo, S. H. *Adv. Energy Mater.* **2016**, *6*, 1501794.
(35) Kramm, U. I.; Herrmann-Geppert, I.; Behrends, J.; Lips, K.; Fiechter, S.; Bogdanoff, P. *J. Am. Chem. Soc.* **2016**, *138*, 635.

DOI: 10.1021/jacs.6b09470
J. Am. Chem. Soc. 2016, 138, 15046−15056

(36) Liang, H.-W.; Wei, W.; Wu, Z.-S.; Müllen, K. *J. Am. Chem. Soc.* **2013**, *135*, 16002.
(37) Wang, J.; Wang, K.; Wang, F.-B.; Xia, X.-H. *Nat. Commun.* **2014**, *5*, 5285.
(38) Wu, Z.-S.; Chen, L.; Liu, J.; Parvez, K.; Liang, H.; Shu, J.; Sachdev, H.; Graf, R.; Feng, X.; Müllen, K. *Adv. Mater.* **2014**, *26*, 1450.
(39) Han, J.; Sa, Y. J.; Shim, Y.; Choi, M.; Park, N.; Joo, S. H.; Park, S. *Angew. Chem., Int. Ed.* **2015**, *54*, 12622.
(40) You, B.; Jiang, N.; Sheng, M.; Drisdell, W. S.; Yano, J.; Sun, Y. *ACS Catal.* **2015**, *5*, 7068.
(41) Xia, B. Y.; Yan, Y.; Li, N.; Wu, H. B.; Lou, X. W.; Wang, X. *Nat. Energy* **2016**, *1*, 15006.
(42) Zheng, Y.; Jiao, Y.; Jaroniec, M.; Jin, Y.; Qiao, S. Z. *Small* **2012**, *8*, 3550.
(43) Wang, D.-W.; Su, D. *Energy Environ. Sci.* **2014**, *7*, 576.
(44) Gong, K.; Du, F.; Xia, Z.; Durstock, M.; Dai, L. *Science* **2009**, *323*, 760.
(45) Liang, J.; Zheng, Y.; Chen, J.; Liu, J.; Hulicova-Jurcakova, D.; Jaroniec, M.; Qiao, S. Z. *Angew. Chem., Int. Ed.* **2012**, *51*, 3892.
(46) Sa, Y. J.; Park, C.; Jeong, H. Y.; Park, S.-H.; Lee, Z.; Kim, K. T.; Park, G.-G.; Joo, S. H. *Angew. Chem., Int. Ed.* **2014**, *53*, 4102.
(47) Liang, H.-W.; Zhuang, X.; Brüller, S.; Feng, X.; Müllen, K. *Nat. Commun.* **2014**, *5*, 4973.
(48) Cheon, J. Y.; Kim, J. H.; Kim, J. H.; Goddeti, K. C.; Park, J. Y.; Joo, S. H. *J. Am. Chem. Soc.* **2014**, *136*, 8875.
(49) Liang, Y.; Li, Y.; Wang, H.; Zhou, J.; Wang, J.; Regier, T.; Dai, H. *Nat. Mater.* **2011**, *10*, 780.
(50) Chen, Z.; Yu, A.; Higgins, D.; Li, H.; Wang, H.; Chen, Z. *Nano Lett.* **2012**, *12*, 1946.
(51) Wu, Z.-S.; Yang, S.; Sun, Y.; Parvez, K.; Feng, X.; Müllen, K. *J. Am. Chem. Soc.* **2012**, *134*, 9082.
(52) Masa, J.; Xia, W.; Sinev, I.; Zhao, A.; Sun, Z.; Grutzke, S.; Weide, P.; Muhler, M.; Schuhmann, W. *Angew. Chem., Int. Ed.* **2014**, *53*, 8508.
(53) Lefèvre, M.; Dodelet, J.-P.; Bertrand, P. *J. Phys. Chem. B* **2000**, *104*, 11238.
(54) Jaouen, F.; Lefèvre, M.; Dodelet, J.-P.; Cai, M. *J. Phys. Chem. B* **2006**, *110*, 5553.
(55) Ziegelbauer, J. M.; Olson, T. S.; Pylypenko, S.; Alamgir, F.; Jaye, C.; Atanassov, P.; Mukerjee, S. *J. Phys. Chem. C* **2008**, *112*, 8839.
(56) Koslowski, U. I.; Abs-Wurmbach, I.; Fiechter, S.; Bogdanoff, P. *J. Phys. Chem. C* **2008**, *112*, 15356.
(57) Kramm, U. I.; Herranz, J.; Larouche, N.; Arruda, T. M.; Lefèvre, M.; Jaouen, F.; Bogdanoff, P.; Fiechter, S.; Abs-Wurmbach, I.; Mukerjee, S.; Dodelet, J.-P. *Phys. Chem. Chem. Phys.* **2012**, *14*, 11673.
(58) Ferrandon, M.; Kropf, A. J.; Myers, D. J.; Artyushkova, K.; Kramm, U.; Bogdanoff, P.; Wu, G.; Johnston, C. M.; Zelenay, P. *J. Phys. Chem. C* **2012**, *116*, 16001.
(59) Grumelli, D.; Wurster, B.; Stepanow, S.; Kern, K. *Nat. Commun.* **2013**, *4*, 2904.
(60) Ramaswamy, N.; Tylus, U.; Jia, Q.; Mukerjee, S. *J. Am. Chem. Soc.* **2013**, *135*, 15443.
(61) Tylus, U.; Jia, Q.; Strickland, K.; Ramaswamy, N.; Serov, A.; Atanassov, P.; Mukerjee, S. *J. Phys. Chem. C* **2014**, *118*, 8999.
(62) Wang, Q.; Zhou, Z.-Y.; Lai, Y.-J.; You, Y.; Liu, J.-G.; Wu, X.-L.; Terefe, E.; Chen, C.; Song, L.; Rauf, M.; Tian, N.; Sun, S.-G. *J. Am. Chem. Soc.* **2014**, *136*, 10882.
(63) Asazawa, K.; Kishi, H.; Tanaka, H.; Matsumura, D.; Tamura, K.; Nishihata, Y.; Saputro, A. G.; Nakanishi, H.; Kasai, H.; Artyushkova, K.; Atanassov, P. *J. Phys. Chem. C* **2014**, *118*, 25480.
(64) Zhu, Y.; Zhang, B.; Liu, X.; Wang, D.-W.; Su, D. S. *Angew. Chem., Int. Ed.* **2014**, *53*, 10673.
(65) Zitolo, A.; Goellner, V.; Armel, V.; Sougrati, M.-T.; Mineva, T.; Stievano, L.; Fonda, E.; Jaouen, F. *Nat. Mater.* **2015**, *14*, 937.
(66) Jia, Q.; Ramaswamy, N.; Hafiz, H.; Tylus, U.; Strickland, K.; Wu, G.; Barbiellini, B.; Bansil, A.; Holby, E. F.; Zelenay, P.; Mukerjee, S. *ACS Nano* **2015**, *9*, 12496.
(67) Artyushkova, K.; Serov, A.; Rojas-Carbonell, S.; Atanassov, P. *J. Phys. Chem. C* **2015**, *119*, 25917.
(68) Jiang, W.-J.; Gu, L.; Li, L.; Zhang, Y.; Zhang, X.; Zhang, L.-J.; Wang, J.-Q.; Hu, J.-S.; Wei, Z.; Wan, L.-J. *J. Am. Chem. Soc.* **2016**, *138*, 3570.
(69) Joo, S. H.; Park, J. Y.; Tsung, C.-K.; Yamada, Y.; Yang, P.; Somorjai, G. A. *Nat. Mater.* **2009**, *8*, 126.
(70) Deng, Y.; Cai, Y.; Sun, Z.; Liu, J.; Liu, C.; Wei, J.; Li, W.; Liu, C.; Wang, Y.; Zhao, D. *J. Am. Chem. Soc.* **2010**, *132*, 8466.
(71) Guerrero-Martínez, A.; Pérez-Juste, J.; Liz-Marzán, L. M. *Adv. Mater.* **2010**, *22*, 1182.
(72) Park, J. C.; Bang, J. U.; Lee, J.; Ko, C. H.; Song, H. *J. Mater. Chem.* **2010**, *20*, 1239.
(73) Zhang, Q.; Lee, I.; Joo, J. B.; Zaera, F.; Yin, Y. *Acc. Chem. Res.* **2013**, *46*, 1816.
(74) Kramm, U. I.; Lefèvre, M.; Larouche, N.; Schmeisser, D.; Dodelet, J.-P. *J. Am. Chem. Soc.* **2014**, *136*, 978.
(75) Mamlouk, M.; Kumar, S. M. S.; Gouerec, P.; Scott, K. *J. Power Sources* **2011**, *196*, 7594.
(76) Rao, C. V.; Ishikawa, Y. *J. Phys. Chem. C* **2012**, *116*, 4340.
(77) He, Q.; Li, Q.; Khene, S.; Ren, X.; López-Suárez, F. E.; Lozano-Castelló, D.; Bueno-López, A.; Wu, G. *J. Phys. Chem. C* **2013**, *117*, 8697.
(78) Ng, J. W. D.; Gorlin, Y.; Nordlund, D.; Jaramillo, T. F. *J. Electrochem. Soc.* **2014**, *161*, D3105.
(79) Lee, S.; Choun, M.; Ye, Y.; Lee, J.; Mun, Y.; Kang, E.; Hwang, J.; Lee, Y.-H.; Shin, C.-H.; Moon, S.-H.; Kim, S.-K.; Lee, E.; Lee, J. *Angew. Chem., Int. Ed.* **2015**, *54*, 9230.
(80) Kim, O.-H.; Cho, Y.-H.; Chung, D. Y.; Kim, M. J.; Yoo, J. M.; Park, J. E.; Choe, H.; Sung, Y.-E. *Sci. Rep.* **2015**, *5*, 8376.
(81) Chen, C.; Yang, X.-D.; Zhou, Z.-Y.; Lai, Y.-J.; Rauf, M.; Wang, Y.; Pan, J.; Zhuang, L.; Wang, Q.; Wang, Y.-C.; Tian, N.; Zhang, X.-S.; Sun, S.-G. *Chem. Commun.* **2015**, *51*, 17092.
(82) Artyushkova, K.; Kiefer, B.; Halevi, B.; Knop-Gericke, A.; Schlogl, R.; Atanassov, P. *Chem. Commun.* **2013**, *49*, 2539.
(83) Kramm, U. I.; Abs-Wurmbach, I.; Herrmann-Geppert, I.; Radnik, J.; Fiechter, S.; Bogdanoff, P. *J. Electrochem. Soc.* **2011**, *158*, B69.
(84) Lim, J. T.; Kim, C. S. *J. Appl. Phys.* **2015**, *117*, 17B743.

DOI: 10.1021/jacs.6b09470
J. Am. Chem. Soc. 2016, 138, 15046−15056